Solution Structure and Backbone Dynamics of the Holo Form of the Frenolicin Acyl Carrier Protein[†,◇]

Qing Li,[‡] Chaitan Khosla,*[,‡,§,||] Joseph D. Puglisi,[⊥,#] and Corey W. Liu[#]

Departments of Chemistry, Chemical Engineering, Biochemistry, and Structural Biology and Stanford Magnetic Resonance Laboratory, Stanford University, Stanford, California 94305

Received December 22, 2002; Revised Manuscript Received February 24, 2003

ABSTRACT: During polyketide biosynthesis, acyl carrier proteins (ACPs) perform the central role of transferring polyketide intermediates between active sites of polyketide synthase. The 4′-phosphopantetheine prosthetic group of a holo-ACP is a long and flexible arm that can reach into different active sites and provide a terminal sulfhydryl group for the attachment of acyl groups through a thioester linkage. We have determined the solution structure and characterized backbone dynamics of the holo form of the frenolicin acyl carrier protein (*fren* holo-ACP) by nuclear magnetic resonance (NMR). Unambiguous assignments were made for 433 hydrogen atoms, 333 carbon atoms, and 84 nitrogen atoms, representing a total of 94.6% of the assignable atoms in this protein. From 879 meaningful NOEs and 45 angle constraints, a family of 24 structures has been calculated. The solution structure is composed of three major α-helices packed in a bundle with three additional short helices in intervening loops; one of the short helices slowly exchanges between two conformations. Superposition of the major helical regions on the mean structure yields average atomic rmsd values of 0.49 ± 0.09 and 0.91 ± 0.08 Å for backbone and non-hydrogen atoms, respectively. Although the three-helix bundle fold is conserved among acyl carrier proteins involved in fatty acid synthases and polyketide synthases, a detailed comparison revealed that ACPs from polyketide biosynthetic pathways are more related to each other in tertiary fold than to their homologues from fatty acid biosynthetic pathways. Comparison of the free form of ACPs (NMR structures of *fren* ACP and the *Bacillus subtilis* ACP) with the substrate-bound form of ACP (crystal structure of butyryl-ACP from *Escherichia coli*) suggests that conformational exchange plays a role in substrate binding.

Polyketide synthases (PKSs) catalyze the biosynthesis of a large and diverse group of pharmacologically important natural products. The carbon chain assembly of polyketides is analogous to fatty acid biosynthesis, in which successive decarboxylative condensation between a growing acyl chain and an α-carboxylated extender unit gives rise to the nascent polyketide chain. Two major types of polyketide synthase systems exist in nature. Type I PKSs are gigantic multifunctional proteins with active sites organized into modules; type II PKSs consist of several monofunctional proteins that are iteratively used in the biosynthetic pathway. The acyl carrier protein (ACP) is a key component to both pathways.

In the type II polyketide synthase system responsible for the biosynthesis of aromatic polyketides (examples shown in Figure 1), acyl carrier proteins are small acidic proteins of approximately 9 kDa. These ACPs tether the growing acyl chains as they migrate between the active sites of PKSs during the course of chain elongation and modification (Figure 2A). Homologues of these proteins, referred to as peptidyl carrier proteins (PCPs), play a related role in nonribosomal peptide biosynthesis. The growing acyl chain is tethered to the ACP via a 4′-phosphopantetheine prosthetic group that is a unique feature of all ACPs. The prosthetic group is covalently attached to a highly conserved serine residue via a phosphodiester linkage and provides a terminal sulfhydryl group for the attachment of acyl groups through

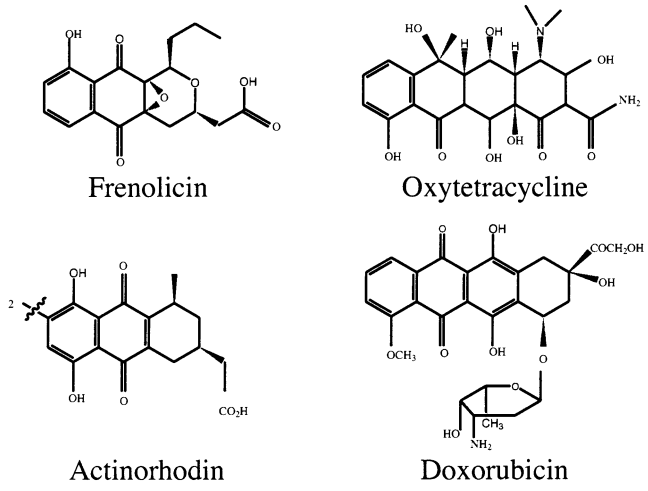

FIGURE 1: Examples of aromatic polyketides.

[†] This research was supported by a grant from the National Institutes of Health (CA 77248 to C.K.). Stanford Magnetic Resonance Laboratory is supported by the Stanford University School of Medicine.

[◇] PDB entry 1OR5.

* Address correspondence to this author at the Department of Chemical Engineering, Stanford University, Stanford, CA 94305-5025. Phone/Fax: 650-723-6538. E-mail: ck@chemeng.stanford.edu.

[‡] Department of Chemistry, Stanford University.

[§] Department of Chemical Engineering, Stanford University.

[||] Department of Biochemistry, Stanford University.

[⊥] Department of Structural Biology, Stanford University.

[#] Stanford Magnetic Resonance Laboratory, Stanford University.

10.1021/bi0274120 CCC: $25.00
Published on Web 04/03/2003

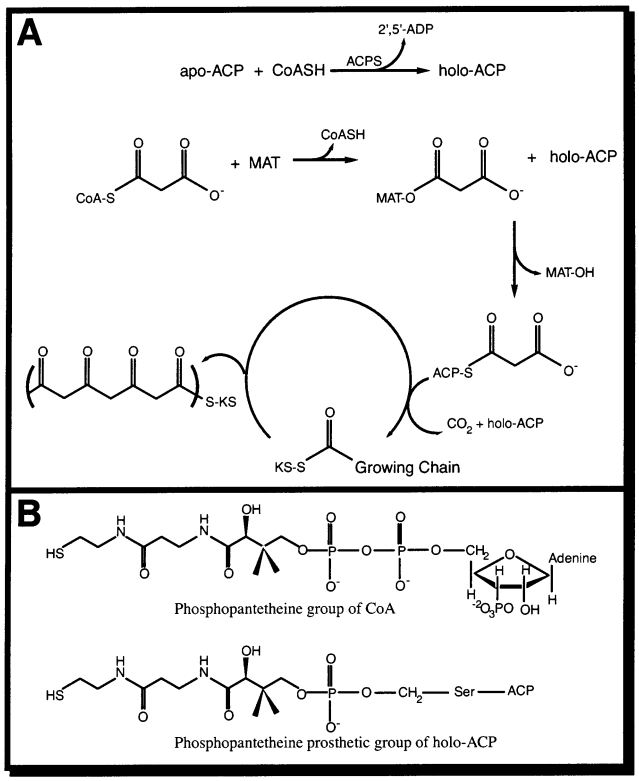

FIGURE 2: (A) Chain elongation steps of polyketide biosynthesis. (B) Phosphopantetheine moiety of CoA and holo-ACP.

a thioester bond (Figure 2B). The 4′-phosphopantetheine moiety is often described as a long and flexible arm that can reach into the active sites of fatty acid synthase (FAS) or polyketide synthase enzymes during chain elongation steps, although direct biophysical evidence for this hypothesis is lacking. The conversion of apo-ACP to holo-ACP requires the activity of a phosphopantetheinyl transferase, such as holo-ACP synthase (ACPS), which recognizes the conserved Asp-Ser-Leu motif in apo-ACPs and transfers the phosphopantetheine moiety from coenzyme A to the serine residue (Figure 2A).

Structural studies of ACPs have been focused more on fatty acid synthase ACPs. NMR solution structures of three FAS ACPs have been determined: *Bacillus subtilis* (*1*) and *Mycobacterium tuberculosis* (*2*) to high resolution and *Escherichia coli* (*3*−*5*) to low resolution. Crystal structures of two FAS ACP systems have been solved as well: a butyryl-acylated holo-ACP from *E. coli* (butyryl-ACP) (*6*) and an ACP−ACPS complex from *B. subtilis* (*7*). The lone structure of an aromatic PKS ACP is that of the apo form of *Streptomyces coelicolor* actinorhodin ACP determined by ^{1}H NMR (*8*). All elucidated structures of ACP exhibit a conserved three-helix bundle motif.

Frenolicin ACP (FrenN) is a well-characterized protein in the type II PKS system. The first biochemical evidence for protein−protein interactions in polyketide biosynthesis was derived from experiments with this ACP (*9*). Extensive biochemical assays have also elucidated the ability of frenolicin ACP to serve as a substrate for *E. coli* holo-ACP synthase (*10*) and its catalytic properties in the hybrid PKS system (*11*, *12*). Given the high sequence homology of aromatic polyketide acyl carrier proteins, the three-dimensional structure of frenolicin ACP should be representative of ACPs in the aromatic PKS system. Here, we have determined the solution structure of frenolicin ACP from *Streptomyces roseofulvus* using high-resolution NMR methods.

The involvement of multiple active sites in fatty acid or polyketide biosynthesis implies that a given ACP must interact with a variety of enzymes to perform its role as a carrier of the acyl chain. The functional flexibility of a protein is often accommodated through conformational flexibility. We have characterized the backbone dynamics of the frenolicin ACP to investigate the structural basis for versatile protein docking as well as the ability to protect the intermediates of various lengths.

In this paper we present the solution structure and backbone dynamics of the holo form of frenolicin ACP. The tertiary structure of the *fren* ACP was compared with those of homologous ACPs reported earlier, including the solution structure of actinorhodin ACP (*act* apo-ACP) (*8*), the *B. subtilis* ACP (*1*), and the recently released crystal structure of butyryl-ACP from *E. coli* (*6*). These comparisons provide excellent explanation to the earlier results of functional analysis of hybrid PKSs and suggest possible biological implications for the conformational exchange observed for a nine amino acid stretch of frenolicin holo-ACP.

MATERIALS AND METHODS

Preparation of Unlabeled and Labeled Protein Samples. The expression of unlabeled *fren* holo-ACP was described previously (*13*). [U-$^{13}C_6$ (99%)]Glucose, [^{15}N (98%+)] ammonium chloride, and [D_{10} (98%)]dithiothreitol (DTT) were purchased from Cambridge Isotope Laboratories. *Fren* apo-ACP was expressed as a uniformly $^{13}C/^{15}N$- or ^{15}N-labeled protein by growing BL21(DE3) cells transformed with plasmid pet21c-*fren*ACP in minimal medium M9 containing 4 g/L [^{13}C]glucose and/or 1 g/L [^{15}N]ammonium chloride at 37 °C. The culture was induced at an OD_{600} of 1.0−1.1 with 1 mM IPTG and incubated at 30 °C overnight. Cells were harvested by centrifugation and lysed by freezing and thawing as previously described (*10*). The ACP was further purified to homogeneity as follows. All purification steps were performed at 4 °C unless otherwise specified. The freeze−thaw supernatant was subjected to ammonium sulfate precipitation, discarding the protein precipitate from the 0−70% fractions. Ammonium sulfate was added to the remaining supernatant to 82.5% saturation, and the supernatant was acidified to pH 4.7 with glacial acetic acid and stirred overnight at 4 °C. Protein precipitate was collected by centrifugation (17000*g*, 90 min, 0 °C). This pellet was dissolved in 10 mL of buffer I (100 mM sodium phosphate, pH 7.3, 2 mM DTT, 2 mM EDTA) and diluted in 40 mL of buffer II (buffer I containing 1.5 M ammonium sulfate). The solution was applied to a phenyl-Sepharose column pre-equilibrated with buffer II. The column was washed with buffer II and developed with a linear 100 mL gradient (1.5−0 M ammonium sulfate in buffer I) at a flow rate of 1 mL/min. Fractions containing *fren* ACP were pooled and concentrated with Centricon tubes (3 kDa cutoff) (Millipore, Inc., Bedford, MA). Proteins were exchanged into buffer III (100 mM sodium phosphate, pH 6.6, 2 mM DTT, 2 mM EDTA) using a PD10 column (Pharmacia).

Apo-ACP was converted into holo-ACP by treatment with catalytic quantities of Sfp [a relatively nonspecific phospho-

pantetheinyl transferase from *B. subtilis* (*14*, *15*)] in the presence of unlabeled CoASH. Reaction conditions were as follows in buffer III: Sfp:ACP = 1:10, 600 μM CoASH, and 10 mM $MgSO_4$. After mixing, the conversion was allowed to go to completion (20 min at 37 °C). The reaction mixture was immediately loaded onto a Resource Q column equilibrated with buffer III. *Fren* holo-ACP was eluted over a 100 mL gradient of 0−0.5 M NaCl at a flow rate of 1 mL/min. The protein was judged to be pure on the basis of SDS−PAGE; electrospray mass spectrometry confirmed 100% conversion to the holo form. These fractions were buffer exchanged into 30 mM sodium phosphate, pH 5.5, and 2 mM [D_{10}]DTT and concentrated with Centricon tubes (3 kDa cutoff). Final NMR samples contained 0.7−1.2 mM *fren* holo-ACP (protein concentration determined by Lowry assay), 2 mM deuterated DTT, and 0.5% NaN_3 in 30 mM sodium phosphate buffer (pH 5.5), containing a 90% H_2O/10% D_2O mixture.

NMR Spectroscopy. All NMR experiments were acquired at the Stanford Magnetic Resonance Laboratory (SMRL) at 15 °C on Varian Inova 500, 600, and 800 MHz spectrometers running VNMR v6.1B or v6.1C (Varian, Inc.) and equipped with 5 mm inverse-detect, triple-resonance $^1H\{^{13}C/^{15}N\}$, pulse-field gradient probes. All data were processed using either VNMR or NMRPipe (*16*) and analyzed with SPARKY (*17*).

Protein resonance assignments and distance constraints were obtained from the following experiments contained within the ProteinPack suite of pulse sequences (Varian, Inc., NMR user library): 3D HNCACB, 3D CCONH, 3D HCCONH, 3D HCCH-TOCSY, 3D HCCH-COSY, 3D ^{15}N NOESY-HSQC (100 ms mixing time), $^{13}C/^{15}N$ 3D NOESY-HSQC (100 ms mixing time), and ^1H 2D NOESY (50 ms mixing time) (*18*−*20*).

Assignments for the 4′-phosphopantetheine prosthetic group were made from 2D ^1H NOESY and TOCSY experiments (ProteinPack) performed on CoASH and an isotope-filtered [F1-C, F2-C]-COSY experiment (*21*) acquired on $^{13}C/^{15}N$-labeled *fren* holo-ACP.

$^3J_{HNH\alpha}$ scalar couplings were determined from analysis of H_N diagonal and H_α cross-peak intensities obtained from a 3D HNHA spectrum (*22*) acquired on a uniformly ^{15}N-labeled *fren* holo-ACP sample.

Heteronuclear ^{15}N T_1 and T_2 relaxation rates and steady-state heteronuclear $^1H-^{15}N$ NOEs were determined from $^1H-^{15}N$ correlation spectra (*23*) collected at 500 MHz. The T_1 experiments were acquired with recycle delays of 5 s and relaxation delays of 10*, 20, 40*, 80, 160, 320*, 640, 1280*, and 2560 ms. The T_2 experiments were acquired with recycle delays of 3 s and relaxation delays of 10*, 30, 70*, 130, and 250* ms. Duplicate measurements were acquired for the indicated (*) relaxation delays. Heteronuclear NOE spectra were acquired with 3 s of on-resonance saturation for the NOE experiment and 3 s recycle delay (no saturation) for the reference spectra.

Slow conformational exchange in *fren* holo-ACP was observed with 2D $^1H-^{15}N$ heteronuclear exchange experiments (*24*) performed at various mixing times (50, 100, 200, 400, and 800 ms).

Structure Determination. Structures were calculated with the torsion angle dynamics approach implemented in DYANA v1.5 (*25*) using 4000 steps per structure. Distance constraint upper bounds were initially generated from NOE data with the CALIBA function of DYANA; phi (ϕ) angle backbone torsion angle restraints were calculated from the $^3J_{HNH\alpha}$ scalar couplings. Constraints were interactively modified to address violations and assignment ambiguities. A total of 30 structures were calculated using the standard simulated annealing protocol found in DYANA. The 24 conformers with the lowest target functions (<0.5) were selected to represent the solution structure ensemble of *fren* holo-ACP. These structures were displayed and analyzed with MOLMOL (*26*). The representative structure of *fren* holo-ACP was obtained using MOLMOL to calculate a mean structure from the superposition of secondary structure elements in the ensemble, followed by application of the standard variable target function minimization implemented in DYANA. Subsequent analysis of the representative structure was performed using DYANA, MOLMOL, and PROCHECK-NMR (*27*).

^{15}N Backbone Dynamics. Cross-peak intensities for all ^{15}N relaxation spectra were determined using SPARKY. T_1 and T_2 relaxation rate constants were obtained by fitting routines within SPARKY. NOE values were obtained by taking the ratio of peak heights between the reference and NOE spectra. The ^{15}N relaxation data were analyzed using the Lipari and Szabo model-free formalism (*28*, *29*) with the program Modelfree v4.15 (*30*, *31*). Selection of the appropriate spectral density functions to model the backbone relaxation behavior was based on previously described criteria (*30*).

RESULTS

Biophysical and Biochemical Characterization of NMR Samples. Protein samples were confirmed to be pure by SDS−PAGE and electrospray mass spectrometry (MS). MS also served to verify 100% conversion of the apo form of *fren* ACP to the holo form. The hydrodynamic radius of the protein was determined by dynamic light scattering to be consistent with a globular, 10.7 kDa protein, indicating that the protein was a monomer under NMR buffer conditions and protein concentrations.

Resonance Assignments. The $^1H-^{15}N$ HSQC spectrum of ^{15}N-labeled *fren* holo-ACP shown in Figure 3 verifies the purity and homogeneity of the protein. Virtually complete sequence-specific backbone and side-chain assignments (95.6% for ^1H, 90.3% for ^{15}N, and 94.6% for ^{13}C) were obtained on the basis of the series of triple-resonance experiments described in the Materials and Methods section.

Side-chain assignments for protons attached to nitrogen atoms in asparagine, glutamine, and arginine residues were deduced from analysis of NOEs to the $^1H\alpha$ and $^1H\beta$ resonances of those residues in ^{15}N-edited NOESY-HSQC and $^{13}C/^{15}N$ NOESY-HSQC spectra.

Several residues in a nine amino acid stretch of the protein (residues 56−64) were found to have two sets of resonances: a major and a minor form of approximately 10:1 distribution. Exchange peaks observed in the ^{15}N-edited NOESY-HSQC spectrum and 2D $^1H-^{15}N$ heteronuclear exchange experiments suggest slow exchange between two different conformations for this stretch, a feature discussed further below. Major form assignments were complete and used in the structure calculations. Poor signal to noise and broad line widths prevented complete assignments of the minor form resonances.

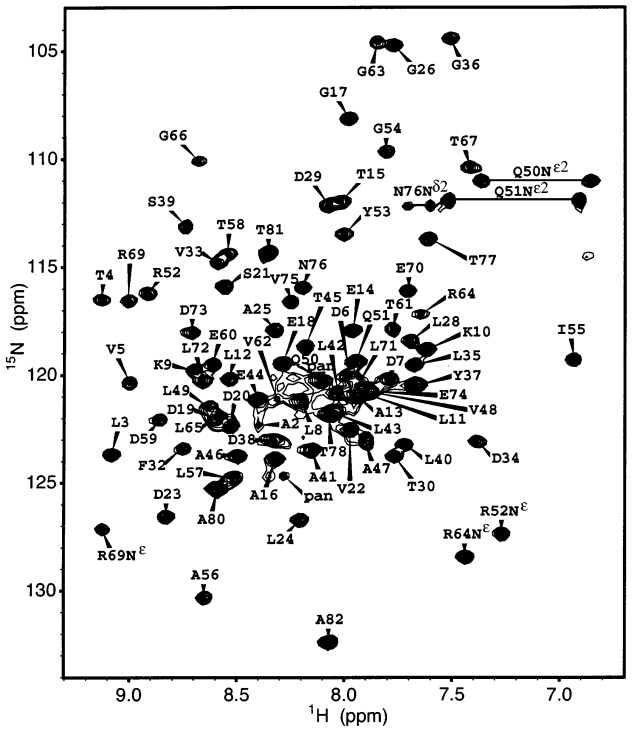

FIGURE 3: 2D ^{1}H−^{15}N HSQC spectrum of frenolicin holo-ACP. Backbone amide resonances are labeled with the one-letter amino acid code and residue number. Pairs of side-chain NH_2 resonances are labeled and connected by horizontal lines. Amides from the phosphopantetheine moiety are labeled as pan.

Secondary Structure. The patterns of short- and medium-range NOEs observed for *fren* holo-ACP are summarized in Figure 4. These secondary structure indicators clearly identify three major helical regions and three short helices in the loop regions.

Quality of the Calculated Structure. A total of 1289 interproton distance constraints and 45 phi (ϕ) angles were used in the structural calculations as summarized in Table 1A. A family of 24 conformers was used to calculate the mean structure. The structural statistics are listed in Table 1B. The structural precision of the ensemble is good with the exception of a long loop (residues 17−38) and short helix (residues 59−63) due to a lack of long-range distance restraints. The overall agreement of the structures with the experimental data is excellent with no upper limit violations greater than 0.40 Å, no van der Waals violations greater than 0.15 Å, and no torsion angle violations larger than 5°. The high quality of the structures is also reflected in good Ramachandran statistics: 71.8% of the (ϕ,ψ) pairs in holo-ACP were found in the most favored regions and 27.8% within the additionally allowed and generously allowed regions (calculated with PROCHECK-NMR).

Tertiary Structure and Charge Distribution of Fren Holo-ACP. Superpositions of the 24 lowest energy structures are shown in Figure 5 along with ribbon representations of the mean structure and its electrostatic surface potentials. The solution structure of *fren* holo-ACP is composed of three major α-helices packed into a bundle with an extended and flexible loop between the first two helices. Helix I (residues 5−16) runs in an antiparallel orientation relative to helices II (residues 39−52) and III (residues 69−77); this helix-bundle topology is well conserved in the ACP

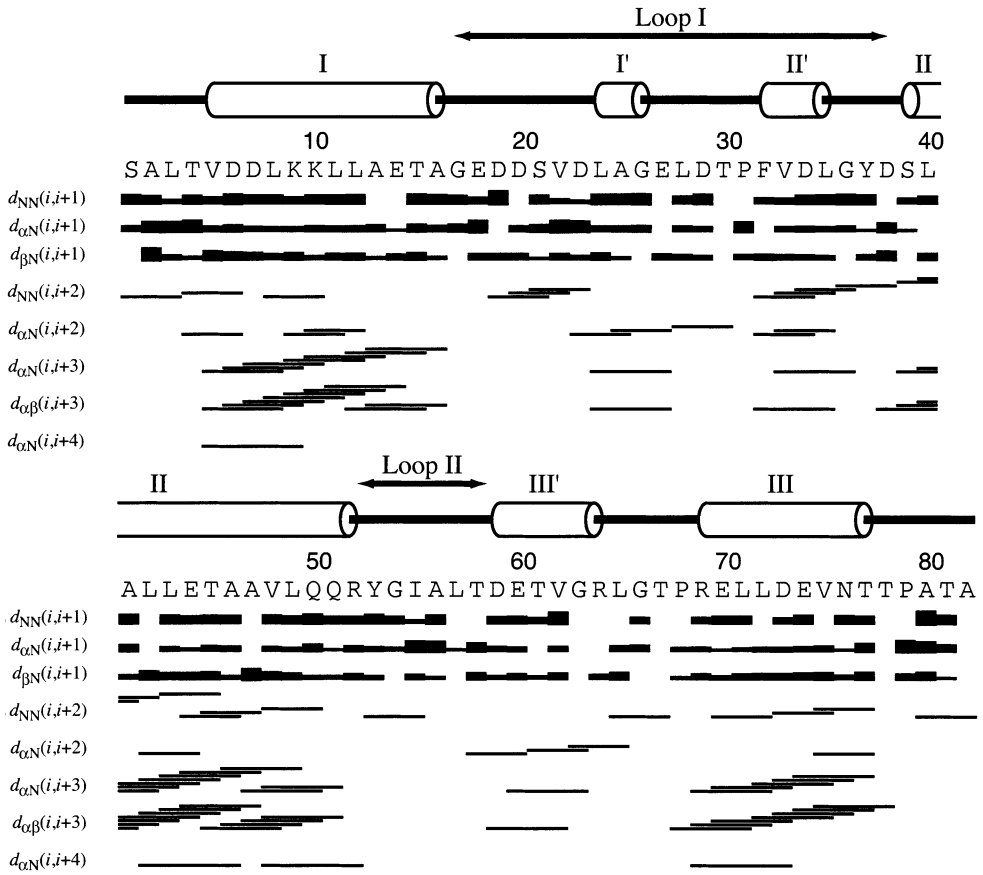

FIGURE 4: Summary of sequential and medium-range NOE patterns for frenolicin holo-ACP. The relative intensities of sequential NOEs are indicated by the heights of the connecting boxes. Medium-range NOEs observed between residue pairs are indicated by horizontal lines. Helical regions are indicated above the amino acid sequence.

Table 1: Structural Statistics of Frenolicin Holo-ACP

(A) NMR-Derived Restraints	
total interproton	1289
intraresidue	410
sequential ($i - j = 1$)	377
short range ($1 < i - j < 5$)	311
long range ($i - j > 4$)	191
total dihedral angles	45
ϕ	45
ψ	0
total no. of restraints	1334
average restraints per residue	16.3

(B1) Structural Quality

	residual violations (24-conformer ensemble)[a]		
	upper limits	van der Waals	torsions
no. of violations [b]	0 ± 0 (0−1)	0 ± 0 (0−0)	0 ± 0 (0−0)
max violation	0.14 ± 0.05 Å (0.06−0.34)	0.11 ± 0.02 Å (0.08−0.14)	0.02 ± 0.01 rad (0.00−0.06)
DYANA target function (Å^2)	0.17 ± 0.07 (0.07−0.34)		

(B2) Structural Quality

Ramachandran statistics[c]	24-conformer ensemble	minimized mean structure
residues in		
most favored regions (%)	71.8	71.2
additional allowed regions (%)	23.9	25.8
generously allowed regions (%)	3.9	3.0
disallowed regions (%)	0.3	0.0

(C) Coordinate Precision of Helical Regions (Å, Mean/Pairwise)[a,d]

N, C$^\alpha$, C′	0.49 ± 0.09 (0.33−0.64)
all heavy atoms	0.91 ± 0.08 (0.79−1.03)

[a] Average values ± standard deviation (minimum value−maximum values). [b] Number of distance restraint violations greater than 0.2 Å (upper limits, van der Waals) and torsion angle restraint violations greater than 5°. [c] Excluding Gly, Pro, and terminal residues (1−2, 78−82). [d] Average rms difference between the 24-conformer ensemble and the minimized mean structure.

family (*1*−*6*, *8*). The packed inner core of the helix bundle is stabilized primarily by hydrophobic residues, with V5, L8, L12, T15, and A16 from helix I, A41, L42, T45, and A46 from helix II, and L71, L72, V75, and N76 from helix III buried inside the helical bundle. The alignment of helices I and II is well defined by numerous NOEs between L12 and L42 and between T15 and T45. A long loop (loop I: residues 17−38) that connects helices I and II is poorly defined at its N-terminal end (residues 17−23) due to a lack of long-range NOEs. The C-terminal end of the loop contains two short helices, helix I′ (residues 24−26, a 3_{10} helix) and helix II′ (residues 32−35), that form a base on which the three-helix bundle sits. The stretch between helices II and III is spanned by a short loop (loop II: residues 53−58), helix (helix III′: residues 59−64), and turn (residues 65−68).

The surface of *fren* ACP is dominated by acidic residues (Figure 5C). Sixteen acidic residues (nine Asp and seven Glu) and five positively charged residues (two Lys and three Arg) contribute to the surface charge distribution. Nearly half of the acidic residues cluster in the long loop I region. Helix III is also more negatively charged than the other two helices, with two glutamic acids and one aspartic acid on the solvent-exposed face.

It has been noted in the *act* ACP structure that two hydrophilic side chains, N79^{act} and R72^{act}, are partially buried (*8*) due to hydrogen-bonding interactions from N79^{act} (γNH$_2$) to L5^{act} (CO) and R72^{act} (ζNH$_2$) to T7^{act} (γO), respectively. In *fren* ACP, a hydrogen bond also exists between N76^{fren} and L3^{fren}, analogous to N79^{act} and L5^{act} (Figure 9A). However, although R69^{fren} (equivalent to R72^{act}) is conserved, V5^{fren} (equivalent to T7^{act}) lacks the γO hydrogen bond acceptor of threonine. Appropriately, in the *fren* ACP the N76 side chain is partially buried while the R69 side chain is solvent exposed.

Conformational Change of the Loop II−*Helix III′ Region.* Four residues in loop II and helix III′ were found to exchange slowly between two conformations on the NMR time scale ($k_{ex} < 10^3$ s^{-1}): alanine 56, threonine 58, aspartate 59, and glycine 63. These residues are highlighted on the structure in Figure 5B. Two sets of chemical shifts were identified for each residue through analysis of ^{15}N-edited NOESY-HSQC, CCONH, and HNCACB experiments. Exchange peaks for the amide protons of these residues were observed in the ^{15}N-edited NOESY-HSQC spectrum and 2D ^{1}H−^{15}N heteronuclear exchange experiments. Figure 6A shows the assignment of the major and minor conformations of the alanine 56 amide while Figure 6B demonstrates the exchange between the two conformations. The exchange lifetime for this process was estimated to be 50−100 ms through analysis of the amide diagonal and off-diagonal cross-peak intensities in the ^{15}N-edited NOESY-HSQC spectrum (*32*).

Backbone Dynamics of Fren Holo-ACP. Relaxation times T_1 and T_2 of ^{15}N and the ^{15}N{^{1}H} NOEs of *fren* holo-ACP were measured and fit to a generalized order parameter, S^2, as described in the Materials and Methods section. Plots of the relaxation data versus the sequence are shown in Figure 7 and summarized in Table 2. Order parameters provide a measure of dynamics of the N−H bond vector: S^2 values ranging from 1.0 for restricted motion to 0.0 for isotropic tumbling. The main three-helix bundle, helices I, II, and III, has an average order parameter of 0.844 ± 0.038, indicating restricted backbone motion for these residues. This is consistent with the well-defined secondary structure for the bundle. The three short helices, I′, II′, and III′, and interhelical residues also have order parameters similar to those of the bundle residues, 0.836 ± 0.026 and 0.832 ± 0.072, respectively. Despite these residues having lower backbone preci-

Table 2: Summary of Heteronuclear ^{15}N Relaxation Parameters for Frenolicin Holo-ACP

	T_1 (s)	T_2 (s)	NOE	S^2
helices I, II, III	0.490 ± 0.014	0.124 ± 0.016	0.726 ± 0.043	0.844 ± 0.038
helices I′, II′, III′	0.495 ± 0.012	0.124 ± 0.042	0.714 ± 0.051	0.836 ± 0.026
coil[a]	0.511 ± 0.035	0.128 ± 0.030	0.693 ± 0.053	0.832 ± 0.072
loop I (17−23)	0.540 ± 0.020	0.184 ± 0.010	0.492 ± 0.038	0.492 ± 0.058
termini[b]	0.629 ± 0.158	0.313 ± 0.207	−0.090 ± 0.804	0.358 ± 0.331

[a] Interhelical residues: 27−31, 36−38, 53−58, and 65−68. [b] Terminal residues: 1−4 and 78−82.

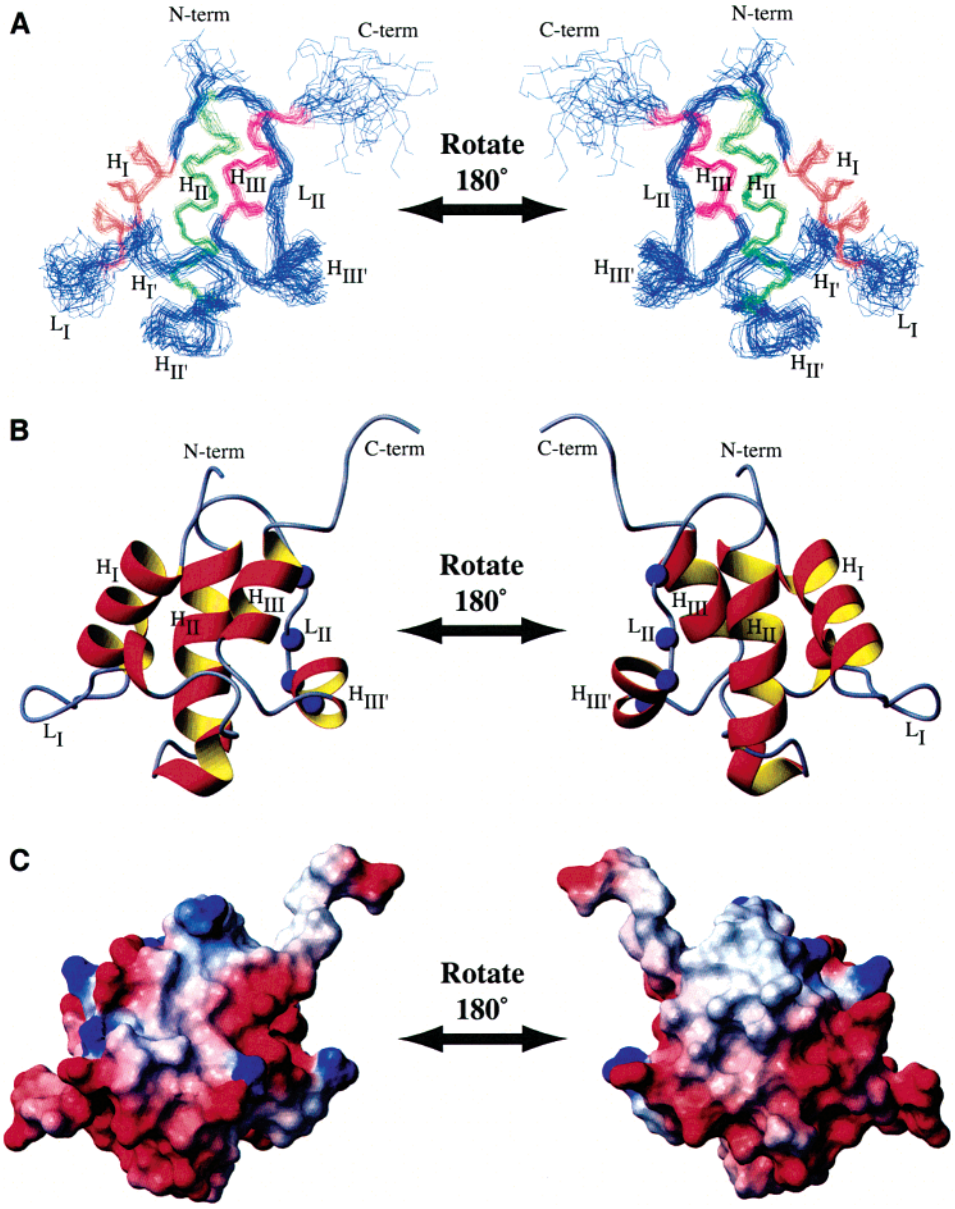

FIGURE 5: NMR structure of frenolicin holo-ACP. (A) Ensemble of 24 torsion angle dynamics conformers, using the backbone atoms of residues 5−16, 39−52, and 69−77 for superposition. (B) Ribbon diagram of the minimized mean structure of frenolicin holo-ACP. (C) Electrostatic potential surface of frenolicin holo-ACP. Positively charged areas are colored in blue, negatively charged areas are in red, and uncharged areas are in gray. Secondary structure elements are labeled as described in the text [helices (HI, HII, HIII, HI′, HII′, HIII′) and loop (LI)]. Residues identified as undergoing slow conformational exchange (alanine 56, threonine 58, aspartate 59, and glycine 63) are shown as blue spheres mapped onto the ribbon diagrams in (B).

sion (Figure 5A), the high order parameters indicate that they do not undergo rapid, large-amplitude internal motions. In contrast, residues 17−23 of loop I have low backbone precision and low order parameters, 0.492 ± 0.058, indicating that this region is dynamic and experiences rapid, large-amplitude motions. The terminal residues also have very low backbone precision and low order parameters, 0.358 ± 0.331, consistent with highly dynamic regions.

Charaterization of the Phosphopantetheine Arm. An isotope-filtered [F1-C, F2-C]-COSY experiment allowed for the observation of only those protons within the 4′-phosphopantetheine prosthetic group. The chemical shifts of these protons were entirely consistent with the chemical shifts of protons of CoASH in the same buffer. The unperturbed chemical shift pattern of the 4′-phosphopantetheine moiety indicates that the prosthetic group has little or transient interaction with the polypeptide.

The assignment process of *fren* ACP resulted in an unidentified amide resonance with signal intensity lower than that of other amides. Analysis of NOEs to this amide proton suggested that it was the thio-terminal amide of the 4′-phosphopantetheine moiety. A natural abundance ^{15}N-HSQC experiment on CoASH confirmed it as one of the amides from the prosthetic group, the other being degenerate with backbone amides. The lower signal intensity of the assigned 4′-phosphopantetheine amide results from an endogenous level of phosphopantetheinylation (30%) during the enriched media expression of *fren* ACP, the remainder being nonisotopically enriched during postexpression modification with natural abundance CoASH.

The heteronuclear ^{15}N relaxation parameters for the 4′-phosphopantetheine amide are T_1 = 1.47 ± 0.20 s, T_2 = 0.68 ± 0.24 s, and NOE = −0.789. The negative NOE in the heteronuclear ^{1}H−^{15}N NOE experiment is shown in

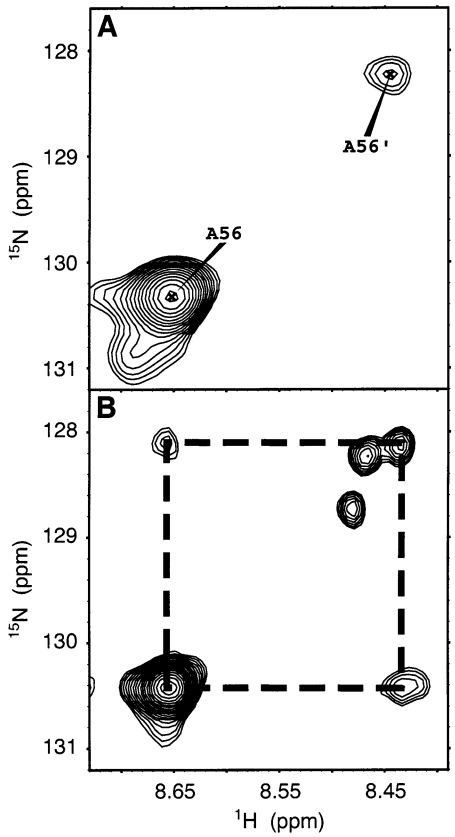

FIGURE 6: Conformational exchange of loop II and helix III′. (A) Region of the ^{1}H−^{15}N HSQC spectrum showing the two amide resonances of alanine 56: the major form, A56, and the minor form, A56′. (B) Same region from a two-dimensional ^{15}N−^{1}H exchange spectrum (100 ms mixing time). The exchange peaks between the major and minor forms of alanine 56 are connected by the dashed box. The remaining two peaks are spurious resonances from sample degradation.

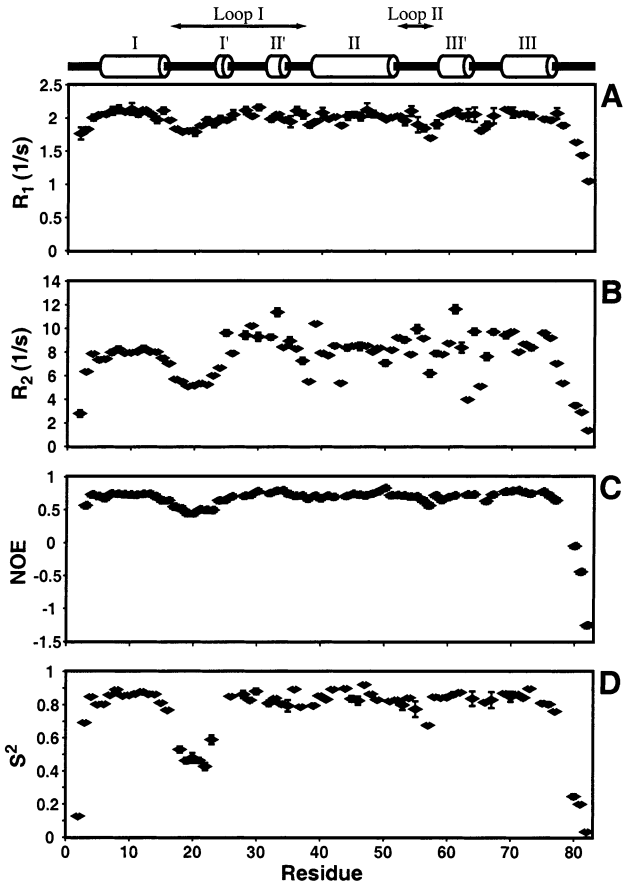

FIGURE 7: ^{15}N relaxation parameters for backbone dynamics analysis of *fren* holo-ACP. (A) R_1 ($1/T_1$), (B) R_2 ($1/T_2$), (C) NOE, and (D) S^2. Secondary structure elements are indicated above the plots. Uncertainties in R_1, R_2, and S^2 were standard deviations resulting from fits of the data to relaxation models (see the text). NOE uncertainties were conservatively estimated to be ±10%.

Figure 8. In comparison to the relaxation parameters for residues in *fren* holo-ACP (Table 2), the long T_1 and T_2 and negative NOE indicate a highly mobile 4′-phosphopantetheine N−H bond vector, consistent with the previous hypothesis of a flexible 4′-phosphopantetheine arm.

DISCUSSION

Only a single structure of an aromatic PKS ACP (actinorhodin ACP) has been previously reported (*8*). The determination of the three-dimensional solution structure of frenolicin ACP increases the database of structural information available to analyze the function of these versatile proteins. *Fren* holo-ACP has a well-defined core structure consisting of a three-helix bundle stabilized by hydrophobic interactions. This core is a highly conserved motif among all ACP proteins and serves as the basis of structural comparisons below. In addition to the core fold, *fren* ACP has regions of conformational flexibility that are suspected to be of functional importance (see below).

Comparison of the Fren Holo-ACP Structure with Other ACP Structures. Acyl carrier proteins are homologous proteins. Amino acid sequence alignments (Figure 9A) indicate that PKS *fren* and *act* ACPs are 57.5% identical (similarity 70.0%) and the FAS *E. coli* ACP and *B. subtilis* ACP are 60.5% identical (similarity 66%). However, when the PKS *fren* ACP is compared to the FAS ACPs, *E. coli* ACP and *B. subtilis* ACP, the percentage of identical residues is 20.7% in both cases. The *M. tuberculosis* ACP is an unusual member in the ACP family with a unique extended C-terminal end (*2*); thus it is not used for structural comparisons with *fren* ACP.

Comparisons of the reported structures of *act* apo-ACP, the *B. subtilis* ACP, and the crystal structure of butyryl-ACP with *fren* holo-ACP indicate that they all have similar secondary structure elements, the three-helix bundle fold being well conserved among acyl carrier proteins. This three-helix bundle topology is also maintained in apo-Dcp and peptidyl carrier proteins (PCPs) (*33*, *34*).

A detailed comparison of tertiary structure is carried out by a superposition of ACPs using the backbone atoms from the conserved three-helix bundles. In Figure 9B the structures of PKS ACPs, *fren* holo-ACP and *act* apo-ACP, are compared, while in Figure 9C the structure of FAS ACPs, *E. coli* butyryl-ACP and *B. subtilis* ACP, are compared. These two superpositions both result in low rmsd values for the three major helices (1.36 Å for the two ACPs in the PKS subfamily and 1.28 Å for the two ACPs in the FAS subfamily). Conformational differences within the helical bundles result from minor variations in the lengths of helices I and III between the ACPs (Figure 9A). Otherwise, the helical orientations are essentially the same within each subfamily. Major differences in tertiary structure are restricted to the two loop regions and the short helix III′.

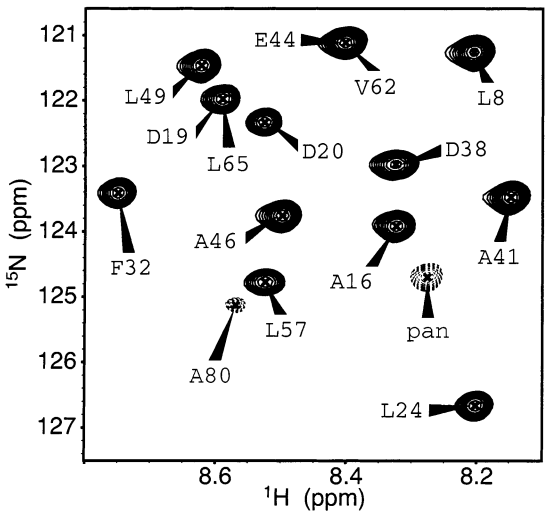

FIGURE 8: Region of ^{15}N heteronuclear NOE spectrum of frenolicin holo-ACP illustrating the conformational flexibility of the phosphopanteteine moiety with respect to the protein backbone. Backbone amide resonances are labeled with the one-letter amino acid code and residue number. The thio-terminal amide from the phosphopantetheine moiety is labeled as pan. Amides with positive heteronuclear NOEs (N−H bond vectors reorienting with the overall tumbling of the molecule) are shown with solid black lines while amides with negative heteronuclear NOEs (N−H bond vectors experiencing rapid, large-amplitude motions with respect to the overall tumbling of the molecule) are shown with dashed gray lines. The pan amide has a large, negative heteronuclear NOE consistent with conformational flexibility, also seen in the A80 amide from the unstructured C-terminus of the protein.

However, when the PKS *fren* ACP is compared to the FAS ACPs, more significant differences are seen. The comparison of *fren* ACP to the *E. coli* butyryl-ACP (Figure 9D) and *B. subtilis* ACP (Figure 9E) yielded noticeably larger rmsd values of 3.13 and 2.80 Å, respectively, in comparison to *fren* ACP with *act* ACP. The positioning and length of the helices between the PKS and FAS subfamilies contribute greatly to the rmsd differences. For *fren* holo-ACP, the N-terminal end of helix I is tilted more toward the hydrophobic core than in the FAS ACPs. This is a result of *fren* ACP having two hydrophobic residues prior to helix I (leucine 3 and valine 5) that stabilize the hydrophobic core (the solvent-accessible areas of leucine 3 and valine 5 are 9.9% and 12.8%, respectively). These hydrophobic residues are conserved in *act* ACP but are absent in the FAS ACPs (Figure 9A). Helix I in the FAS ACPs is also roughly one turn longer than helix I in *fren* ACP and *act* ACP. Helix III of *fren* ACP runs antiparallel with respect to helix I and is oriented to maintain a hydrogen bond between the two helices [leucine 3 (NH) to asparagine 76 (γCO)]. This feature is conserved in *act* ACP but absent in the FAS ACPs due to the lack of a hydrogen bond donor at the N-terminal end. The length of helix II is the most consistent among the three major helices, likely related to its function as a recognition site for holo-ACP synthase and critical to the role of ACP in presenting the active serine for phosphopantetheinylation.

The structural homologies of ACPs reflect their sequence and functional homologies. The sequence and functional

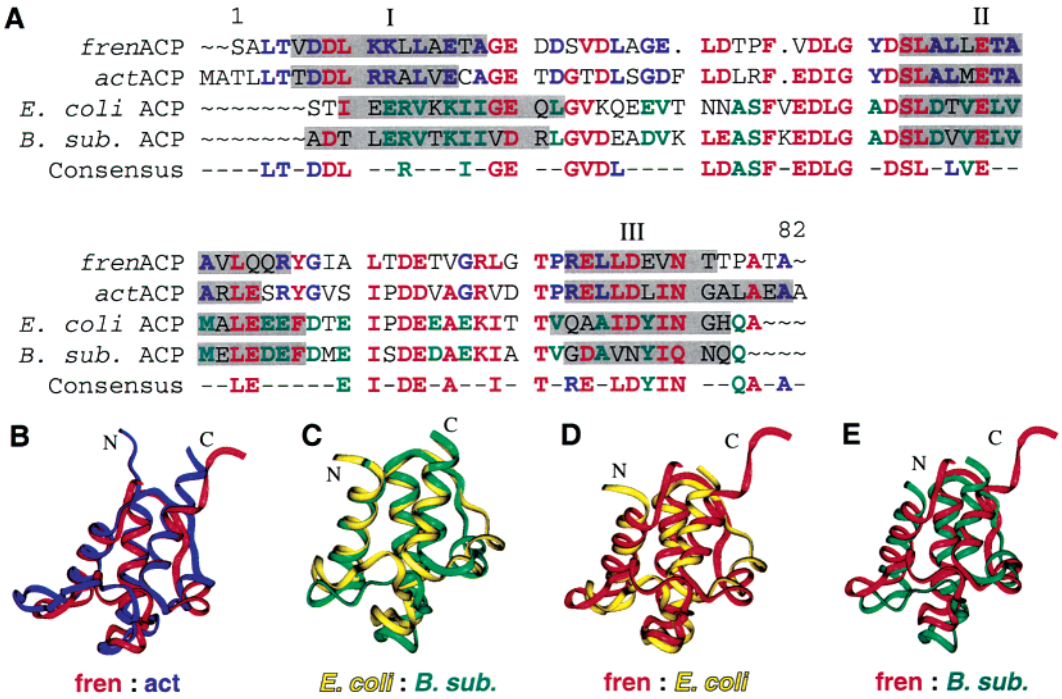

FIGURE 9: Comparison of frenolicin holo-ACP structure to other ACPs (*fren*ACP = frenolicin holo-ACP, *act*ACP = actinorhodin ACP, *E. coli* ACP = *E. coli* butyryl-ACP, and *B. sub.* ACP = *B. subtilis* ACP). (A) Sequence alignment of different ACPs. Residues that are conserved in three or all ACPs are colored in red, residues conserved between *fren* and *act* ACPs are in blue, residues conserved between *E. coli* ACP and *B. subtilis* ACP are in green. Helices from the three-helix bundle are shaded and labeled. (B−E) Structure comparison of different ACPs by superimposing backbone (N, C$^{\alpha}$, and C′) atoms in helical regions. (B) *act* apo-ACP (PDB entry 2AF8, blue) was superimposed on *fren* holo-ACP (red) using residues 5−16, 39−52, and 69−77, with a resulting backbone rmsd of 1.36 Å. (C) *E. coli* butyryl-ACP (PDB entry 1L0H, yellow) was superimposed on *B. subtilis* ACP (PDB entry 1HY8, green) using residues 3−12, 37−49, and 66−74, with a resulting backbone rmsd of 1.28 Å. (D) *E. coli* butyryl-ACP (yellow) was superimposed on *fren* holo-ACP (red) using residues 8−16, 40−52, and 69−77, with a resulting backbone rmsd of 3.13 Å. (E) *B. subtilis* ACP (green) was superimposed on *fren* holo-ACP (red) using residues 8−16, 39−52, and 69−77, with a resulting backbone rmsd of 2.80 Å.

similarities within the ACP members of the PKS and FAS subfamilies are clear. Hence, it is not surprising that the tertiary fold of *fren* ACP is more similar to its PKS subfamily homologue, *act* ACP, than it is to the FAS subfamily ACPs *E. coli* ACP and *B. subtilis* ACP. The structural differences between families also helps to explain the quantitative production difference in hybrid PKS assays containing heterologous ACPs (*11*, *12*). Functional analysis of hybrid polyketide synthases revealed that FAS ACP of *S. erythraea* could functionally replace *act* ACP, but the enzyme activity was significantly reduced, whereas replacement of *act* ACP with *fren* ACP resulted in a comparable level of polyketide production.

Biological Implications of ACP Dynamics. The second loop and short helix (loop II and helix III′) of *fren* ACP were found to exist in two conformations in slow exchange on the NMR time scale (50−100 ms). The relatively large chemical shift differences for the amide proton of alanine 56 and glycine 63 suggest that the two conformers experience quite different local environments. In 1989, a dynamic two-state model for *E. coli* ACP was proposed by Kim and Prestegard (*35*). It was hypothesized in this model that the protein consists of two conformers in dynamic equilibrium and the instability of helix II as suggested by amide exchange rate and spin relaxation time data may be responsible for the mobility needed for the conversion between the two conformers. A similar two-state interconversion was also observed for spinach ACP-I (*36*). However, NMR structural studies of all other ACPs published so far failed to reveal similar features of conformational exchange. Our observation of the two conformational states for this short helix is therefore of special interest to the studies of dynamic properties of ACPs. A close examination of the corresponding region in the *act* ACP structure ensemble revealed that this region has a relatively large backbone rmsd. The short helix is present in only a few structures in the 24 structure ensemble while only a short loop showing some helical propensity was found in the other structures. The poor definition of this region may reflect the dynamic property of this region in *act* ACP as well. Because spectroscopic data for the *act* ACP were acquired with unlabeled protein using homonuclear NMR techniques, it would be difficult to detect the conformational exchange peaks in 2D NOESY spectra. The generality of loop II and helix III′ dynamics in other ACPs merits further investigation.

Structural analysis and comparison of ACPs suggest the importance of conformational flexibility in incorporating the acyl group. The crystal structure of *E. coli* butyryl-ACP revealed two crystal forms (*6*): one with a hydrophobic cavity in the vicinity of the phosphopantetheinylated Ser36 containing partial electron density of the butyrylated prosthetic group and a second with a contracted cavity lacking any density from the prosthetic group. A surface representation of the butyrylated prosthetic group in the binding cavity is shown in Figure 10A. The cavity is comprised primarily of residues in the surrounding helix II, helix III, and helix III′ (*fren* ACP secondary element notations). The same region of the *fren* ACP structure (Figure 10B) and the *B. subtilis* ACP structure (not shown) shows only a narrow cleft of insufficient width to accommodate a butyryl group (Figure 10B). Of particular note between butyryl-ACP and *fren* ACP are the differences in helix III′ position with respect to helix

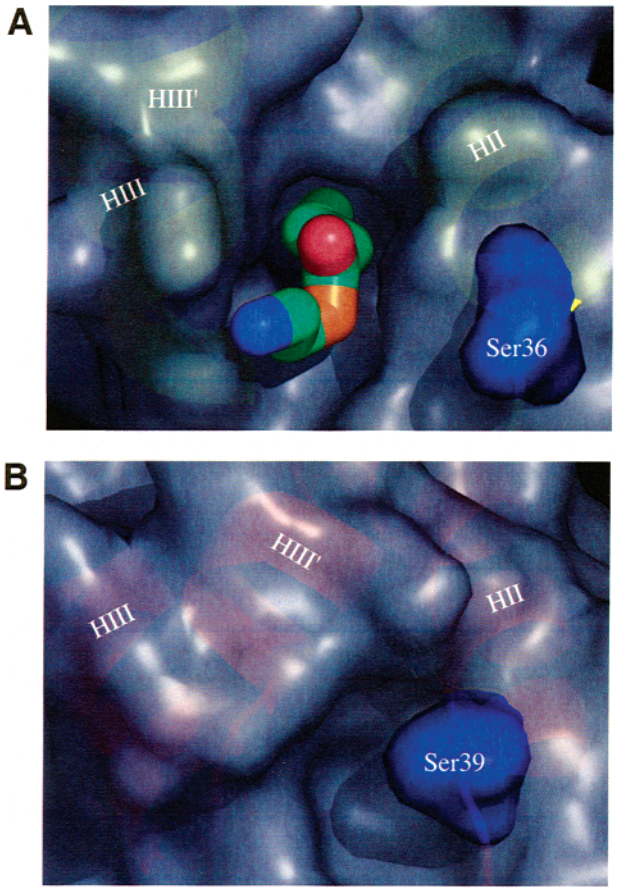

FIGURE 10: (A) The acyl butyryl binding cavity of *E. coli* butyryl-ACP. (B) The same region of *fren* ACP. Shown are translucent surfaces of the regions with labeled ribbon diagrams of the underlying secondary structure components. The conserved active site serines are labeled and highlighted in blue. The butyryl group in (A) is represented in stick form. Figures were generated using PyMol v.0.82 (*39*).

II and helix III. This is likely the primary structural determinant of the size of the binding cavity. Helix III′ of *fren* ACP is close to the helical bundle, making the purported binding cavity too small to accommodate substrate. It is therefore very likely that the conformational change observed in the loop II and helix III′ regions is important for facilitating insertion of acyl group substrates as well as the phosphopantetheine arm when substrate is attached. This flexible region exists predominantly in the "closed" conformation for the free form of ACP with the loop II/helix III′ flap close to the major helices as determined from the NMR structures of both *fren* ACP and *B. subtilis* ACP. This flap may swing away from the helical bundle to adopt an "open" conformation when the phosphopantetheine group, which originally extends into solution, is tethered to the acyl group and inserts into the hydrophobic pocket. This hypothesis is consistent with the two contributing conformations seen in the crystallographic studies of *E. coli* butyryl-ACP where the main differences between the two forms are primarily seen in the regions containing loop II and helix III′.

Finally, conformational flexibility in *fren* ACP may be required for its interaction with other proteins in PKS. Frenolicin ACP interacts with at least three different enzymes. First, a phosphopantetheinyl transferase converts the apoprotein into the active holo form. This holo-ACP must then interact with an acyl transferase to facilitate transfer of

a malonyl group from malonyl-CoA to its phosphopantetheine arm. Finally, malonyl-ACP must interact with the ketosynthase (or an acyl-S-ketosynthase intermediate) to catalyze chain initiation or elongation (Figure 2A). In addition to having appropriate sites on the protein surface to serve as docking interfaces with other proteins, a certain degree of conformational flexibility may also be required in the ACP to interact with different enzymes. The relatively dynamic portion of the first loop and the short helix in conformational exchange may provide the protein the required mobility to accomplish the interface docking.

Recent studies of protein−protein interactions in fatty acid and polyketide biosynthesis using various methods such as crystallography (*7*), docking simulation, and mutagenesis (*37*, *38*) have shown that the highly conserved helix II is recognized by the ACPS and the ketosynthase (*7*, *37*) and that the docking site for MAT is the conserved DSL motif and the short helix in the loop region (*38*). Examination of the frenolicin ACP structure showed that the specific residues involved in the protein−protein interactions are all solvent exposed. These data show that the high-resolution structure of *fren* ACP will provide the basis for future biochemical and modeling studies of ACPs.

ACKNOWLEDGMENT

We gratefully acknowledge Drs. Yunjun Wang, Stephen Lynch, and Scott Blanchard for valuable discussions and generous help. We also thank Dr. Sheryl Tsai for help with dynamic light scattering analysis.

SUPPORTING INFORMATION AVAILABLE

Three tables providing NMR resonance assignments of *fren* ACP and the 4′-phosphopantetheine prosthetic group and heteronuclear ^{15}N backbone relaxation and order parameters and one figure showing the structure of the 4′-phosphopantetheine prosthetic group labeled as assigned in Table 2 of the Supporting Information. This material is available free of charge via the Internet at http://pubs.acs.org.

REFERENCES

1. Xu, G. Y., Tam, A., Lin, L., Hixon, J., Fritz, C. C., and Powers, R. (2001) *Structure 9*, 277−287.
2. Wong, H. C., Liu, G. H., Zhang, Y. M., Rock, C. O., and Zheng, J. (2002) *J. Biol. Chem. 277*, 15874−15880.
3. Holak, T. A., Kearsley, S. K., Kim, Y., and Prestegard, J. H. (1988) *Biochemistry 27*, 6135−6142.
4. Holak, T. A., Nilges, M., Prestegard, J. H., Gronenborn, A. M., and Clore, G. M. (1988) *Eur. J. Biochem. 175*, 9−15.
5. Kim, Y., and Prestegard, J. H. (1990) *Proteins 8*, 377−385.
6. Roujeinikova, A., Baldock, C., Simon, W. J., Gilroy, J., Baker, P. J., Stuitje, A. R., Rice, D. W., Slabas, A. R., and Rafferty, J. B. (2002) *Structure 10*, 825−835.
7. Parris, K. D., Lin, L., Tam, A., Mathew, R., Hixon, J., Stahl, M., Fritz, C. C., Seehra, J., and Somers, W. S. (2000) *Struct. Folding Des. 8*, 883−895.
8. Crump, M. P., Crosby, J., Dempsey, C. E., Parkinson, J. A., Murray, M., Hopwood, D. A., and Simpson, T. J. (1997) *Biochemistry 36*, 6000−6008.
9. Dreier, J., Shah, A. N., and Khosla, C. (1999) *J. Biol. Chem. 274*, 25108−25112.
10. Gehring, A. M., Lambalot, R. H., Vogel, K. W., Drueckhammer, D. G., and Walsh, C. T. (1997) *Chem. Biol. 4*, 17−24.
11. Khosla, C., Ebert-Khosla, S., and Hopwood, D. A. (1992) *Mol. Microbiol. 6*, 3237−3249.
12. Khosla, C., McDaniel, R., Ebert-Khosla, S., Torres, R., Sherman, D. H., Bibb, M. J., and Hopwood, D. A. (1993) *J. Bacteriol. 175*, 2197−2204.
13. Carreras, C. W., Gehring, A. M., Walsh, C. T., and Khosla, C. (1997) *Biochemistry 36*, 11757−11761.
14. Lambalot, R. H., Gehring, A. M., Flugel, R. S., Zuber, P., LaCelle, M., Marahiel, M. A., Reid, R., Khosla, C., and Walsh, C. T. (1996) *Chem. Biol. 3*, 923−936.
15. Quadri, L. E. N., Weinreb, P. H., Lei, M., Nakano, M. M., Zuber, P., and Walsh, C. T. (1998) *Biochemistry 37*, 1585−1595.
16. Delaglio, F., Grzesiek, S., Vuister, G. W., Zhu, G., Pfeifer, J., and Bax, A. (1995) *J. Biomol. NMR 6*, 277−293.
17. Goddard, T. D., and Kneller, D. G. (2002) SPARKY 3, University of California, San Francisco.
18. Sattler, M., Schleucher, J., and Griesinger, C. (1999) *Prog. Nucl. Magn. Reson. Spectrosc. 34*, 93−158.
19. Ferentz, A. E., and Wagner, G. (2000) *Q. Rev. Biophys. 33*, 29−65.
20. Kanelis, V., Forman-Kay, J. D., and Kay, L. E. (2001) *IUBMB Life 52*, 291−302.
21. Ikura, I., and Bax, A. (1992) *J. Am. Chem. Soc. 114*, 2433−2440.
22. Kuboniwa, H., Grzesiek, S., Delaglio, F., and Bax, A. (1994) *J. Biomol. NMR 4*, 871−878.
23. Farrow, N. A., Muhandiram, R., Singer, A. U., Pascal, S. M., Kay, C. M., Gish, G., Shoelson, S. E., Pawson, T., Forman-Kay, J. D., and Kay, L. E. (1994) *Biochemistry 33*, 5984−6003.
24. Farrow, N. A., Zhang, O. W., Forman-Kay, J. D., and Kay, L. E. (1994) *J. Biomol. NMR 4*, 727−734.
25. Güntert, P., Mumenthaler, C., and Wüthrich, K. (1997) *J. Mol. Biol. 273*, 283−298.
26. Koradi, R., Billeter, M., and Wüthrich, K. (1996) *J. Mol. Graphics 14*, 51−55.
27. Laskowski, R. A., Rullmann, J. A. C., MacArthur, M. W., Kaptein, R., and Thornton, J. M. (1996) *J. Biomol. NMR 8*, 477−486.
28. Lipari, G., and Szabo, A. (1982) *J. Am. Chem. Soc. 104*, 4546−4559.
29. Lipari, G., and Szabo, A. (1982) *J. Am. Chem. Soc. 104*, 4559−4570.
30. Mandel, A. M., Akke, M., and Palmer, A. G. (1995) *J. Mol. Biol. 246*, 144−163.
31. Palmer, A. G., Rance, M., and Wright, P. E. (1991) *J. Am. Chem. Soc. 113*, 4371−4380.
32. Baine, P. (1986) *Magn. Reson. Chem. 24*, 304−307.
33. Volkman, B. F., Zhang, Q. Y., Debabov, D. V., Rivera, E., Kresheck, G. C., and Neuhaus, F. C. (2001) *Biochemistry 40*, 7964−7972.
34. Weber, T., Baumgartner, R., Renner, C., Marahiel, M. A., and Holak, T. A. (2000) *Struct. Folding Des. 8*, 407−418.
35. Kim, Y., and Prestegard, J. H. (1989) *Biochemistry 28*, 8792−8797.
36. Kim, Y. M., and Prestegard, J. H. (1990) *J. Am. Chem. Soc. 112*, 3707−3709.
37. Zhang, Y.-M., Rao, M. S., Heath, R. J., Price, A. C., Olson, A. J., Rock, C. O., and White, S. W. (2001) *J. Biol. Chem. 276*, 8231−8238.
38. Keatinge-Clay, A. T., Shelat, A. A., Savage, D. F., Tsai, S. C., Miercke, L. J. W., O'Connell, J. D., Khosla, C., and Stroud, R. M. (2003) *Structure 11*, 147−154.
39. DeLano, W. L. (2002) The PyMOL Molecular Graphics System, DeLano Scientific, San Carlos, CA.

BI0274120